

Global and Local Infall in the ASHES Sample (GLASHES). II. Asymmetric Line Profiles around Dense Cores in 70 μm Dark Massive Clumps

KAHO MORII ^{1,*} PATRICIO SANHUEZA ² QIZHOU ZHANG ¹ AND JAMES M. JACKSON ^{3,4,5}

¹*Center for Astrophysics | Harvard & Smithsonian, 60 Garden Street, Cambridge, MA 02138, USA*

²*Department of Astronomy, School of Science, The University of Tokyo, 7-3-1 Hongo, Bunkyo-ku, Tokyo 113-0033, Japan*

³*Green Bank Observatory, 155 Observatory Road, Green Bank, WV 24944, USA*

⁴*USRA SOFIA Science Center, NASA Ames Research Center, Moffett Field, CA 94045, USA*

⁵*School of Mathematical and Physical Sciences, University of Newcastle, University Drive, Callaghan, NSW 2308, Australia*

ABSTRACT

Gravitational collapse is fundamental to star formation, yet direct kinematic evidence of infall at the core scale in high-mass star-forming regions remains poorly constrained. We present the first large-scale statistical study of infall signatures in 304 dense cores within 24 massive 70 μm -dark clumps from the GLASHES (Global and Local Infall in the ASHES Sample) survey. Using ALMA Band 6 observations of the optically thick tracers HCO⁺ and HNC ($J=3-2$), we systematically characterize blue asymmetry line profiles indicative of infalling motions. We employ two complementary metrics, the velocity difference parameter (δ_v) and the asymmetry parameter (A), to quantify infall signatures, finding consistent results across both tracers. Blue asymmetry profiles are detected in ~ 50 -60% of cores ($\delta_v < 0$ or $A > 0$). Spectral classification reveals that $\sim 60\%$ of cores exhibit double-peaked profiles, and 34% and 39% show blue asymmetry profiles in HCO⁺ and HNC, respectively, with the percentage increasing with core mass and surface density. Accounting for geometric effects that can obscure infall signatures, our results suggest that gravitational collapse is prevalent in and around the cores. Importantly, infall signatures are detected from the prestellar stage and become more dominant as cores' evolution proceeds. Even cores with virial parameters $\alpha_{vir} > 2$ show infall signatures, suggesting that external compression may trigger collapse in addition to self-gravity or that linewidth may include inward motion in addition to turbulence. Furthermore, a moderate correlation between clump-scale and core-scale asymmetry supports a hierarchical collapse scenario, implying a dynamic and multi-scale process of high-mass star formation.

Keywords: Infrared dark clouds (787) — Star formation (1569) — Star forming regions (1565)

1. INTRODUCTION

Gravitational collapse is the fundamental process driving the formation of stars. As comprehensively reviewed by N. J. Evans (1999) and N. J. Evans (2003), identifying the kinematic signatures of this collapse is crucial for understanding the earliest stages of star formation. Specifically, the “blue asymmetry” profile, a line profile with brighter emission on the blue side, observed in optically thick molecular lines toward central dense regions, provides direct spectroscopic evidence of infalling gas motions (e.g., J. M. Jackson et al. 2019). Such a profile is produced when the excitation temperature increases

toward the center of the structure (e.g., cloud, clumps, or cores). This signature has been observed for about five decades across a wide range of environments, including molecular clouds (C. M. Leung & R. L. Brown 1977; P. C. Myers et al. 1996), dense cores in nearby low-mass star-forming regions (S. Zhou et al. 1993; M. Tafalla et al. 1998; C. W. Lee & P. C. Myers 2011; J. L. Campbell et al. 2016), dense cores in high-mass star-forming regions (T. Csengeri et al. 2011; Y. Contreras et al. 2018; K. Morii et al. 2025; S. Gupta et al. 2026), high-mass protostellar cores (P. T. P. Ho & A. D. Haschick 1986; E. R. Keto et al. 1988; Q. Zhang et al. 1998; G. A. Fuller et al. 2005), massive clumps (P. Sanhueza et al. 2010; N. Schneider et al. 2010; M. Reiter et al. 2011; K. L. J. Rygl et al. 2013; Y.-X. He et al. 2016; F. Wyrowski et al. 2016; A. Traficante et al. 2017; J. M. Jackson et al. 2019; Y.

Email: kaho.morii@cfa.harvard.edu

* CfA Postdoctoral Fellow

Yang et al. 2021; F. Xu et al. 2023; J. M. Jackson et al. 2026), and (UC)HII regions (Q. Zhang & P. T. P. Ho 1997). However, while infall has been well characterized at the core scale ($\sim 0.01\text{--}0.1$ pc) in nearby low-mass star-forming regions, direct kinematic evidence at the same scale in high-mass star-forming regions remains limited to some case studies.

Understanding infall in high-mass star formation is of particular importance in the context of current theoretical frameworks. Models such as the “clump-fed” accretion scenario (e.g., I. A. Bonnell et al. 2004; P. Wang et al. 2010; P. Padoan et al. 2020) including the Global Hierarchical Collapse (GHC) model (E. Vázquez-Semadeni et al. 2019) predict that gas inflow or infall is continuous from the parent molecular cloud down to individual cores, implying that core-scale infall is a direct result of large-scale dynamical accretion. Characterizing infall at the core scale is therefore essential to validate these scenarios and to understand how high-mass stars accumulate sufficient mass. However, observational verification at the core scale in high-mass star-forming regions presents significant challenges due to their typically large distances ($\gtrsim 3$ kpc) and highly clustered environments, and previous studies have largely been limited to coarse spatial resolutions at the clump scale (~ 1 pc), or to a handful of particularly bright massive protostars and (UC)HII regions.

At the clump scale, large surveys such as MALT90 (J. B. Foster et al. 2011; J. M. Jackson et al. 2013) have successfully identified global infall motions (e.g., J. M. Jackson et al. 2019), and suggest that infall is particularly active in earlier evolutionary stages, including infrared dark clouds (IRDCs; K. M. Menten et al. 2005; T. K. Sridharan et al. 2005; J. M. Rathborne et al. 2006; E. T. Chambers et al. 2009; P. Sanhueza et al. 2012, 2013, 2017; K. Morii et al. 2021). Although some interferometric studies have inferred gas inflow from velocity gradients in IRDCs (e.g., T. Csengeri et al. 2011; H. Beuther et al. 2013; J. D. Henshaw et al. 2014; X. Lu et al. 2018; H.-R. V. Chen et al. 2019; P. Sanhueza et al. 2021; E. Redaelli et al. 2022; P. Sanhueza et al. 2025), direct kinematic evidence of gravitational collapse via blue asymmetry at the core scale has been reported in only a few individual case studies (e.g., T. Csengeri et al. 2011; Y. Contreras et al. 2018; K. Morii et al. 2025). A comprehensive statistical understanding of core-scale infall in the earliest stages of high-mass star formation therefore remains lacking.

To address this observational gap, the “Global and Local Infall in the ASHES Sample” (GLASHES) survey targets 70 μm dark massive clumps identified in the ALMA Survey of 70 μm Dark High-mass Clumps

in Early Stages (ASHES; P. Sanhueza et al. 2019; K. Morii et al. 2023), which represent ideal laboratories for studying the initial conditions of high-mass star formation (e.g., S. Li et al. 2020; D. Tafuya et al. 2021; T. Sakai et al. 2022; S. Li et al. 2022; G. Sabatini et al. 2022; S. Li et al. 2023; N. Izumi et al. 2024; K. Morii et al. 2024; S. Lin et al. 2025; K. Morii et al. 2026). In our pilot study in one of the ASHES targets, G337.54, hosting 17 cores (K. Morii et al. 2025), we established a robust methodology to extract core-scale infall signatures, derived infall velocities, and confirmed that they are higher than those found in nearby low-mass star-forming regions. Following it, this study extends the analysis to 24 massive clumps containing 304 dense cores to provide the first large-scale statistical evidence of gravitational collapse in the earliest stages of high-mass star formation. The primary goal of this paper is to report the detection rates of blue asymmetry across a large sample and to rigorously evaluate the classification criteria using multiple metrics. We also investigate how the frequency of these signatures relates to core properties and the surrounding clump environment. Detailed radiative transfer modeling to derive quantitative infall rates and other physical parameters will be presented in a subsequent paper. We describe the observational setup in Section 2, present the line emission results and methods for profile characterization and spectral classification in Section 3, discuss the detection rates and correlations with core and clump properties in Section 4, and summarize our findings in Section 5.

2. OBSERVATIONS AND DATA REDUCTION

The GLASHES project consists of data from Band 3 and 6 taken with the main 12-m array, and the Atacama Compact Array (ACA), including both the 7-m array and Total Power (TP) array. The observations have been done during Cycles 6 (2018.1.00299.S, PI: Y. Contreras), 10 (2023.1.01150.S, PI: K. Morii), and 11 (2024.1.01505.S, PI: K. Morii). Targets are 24 massive clumps selected from the ASHES sample, which contains at least one sub-virial ($\alpha_{\text{vir}} < 2$), intermediate-mass cores ($M > 4 M_{\odot}$). The correlator setup covered HCO⁺ ($J = 3 - 2$, $\nu = 267.557633$ GHz), HNC ($J = 3 - 2$, $\nu = 271.981111$ GHz) and HC¹⁸O⁺ ($J = 3 - 2$, $\nu = 255.479$ GHz in Band 6 and N₂H⁺ ($J = 1 - 0$, $\nu = 93.173763$ GHz) in Band 3. In this paper, we mainly use Band 6 data. N₂H⁺ data was used only for determining the systemic velocity (see Appendix A).

The ALMA 12 m array consisted of 41–47 antennas, with a baseline ranging from 15 to 313 m and 779 m for Band 6 and Band 3, respectively. The total on-source time was $\sim 7\text{--}20$ minutes. These observations are sen-

sitive to angular scales smaller than $\sim 10''$ and $\sim 15''$ for Band 6 and Band 3, respectively. More extended emission was recovered by including ACA data. The 7 m array observations consisted of 8–11 antennas, with baselines ranging from 5 to 48 m. The total on-source time was ~ 50 – 97 minutes for Band 6 and ~ 29 – 58 minutes for Band 3. These observations are sensitive to angular scales smaller than $\sim 25''$ and $\sim 72''$ for Band 6 and Band 3, respectively. We also obtained total power data to cover the zero-baseline information. The total power array consisted of three antennas, and the total on-source time was ~ 300 minutes and ~ 250 minutes for Band 6 and Band 3, respectively. All observations have been done in single-pointing. Such observation setup (observation dates, baseline, number of antennas, and total on-source time) is summarized in Table 1.

Data reduction was carried out using CASA software package versions 6.5.4.9 and 6.6.1.17 for calibration and 6.6.3-22 for imaging (CASA Team et al. 2022). After subtracting continuum emission, we combined the 12 m array data with the 7 m array data and cleaned together. After that, we combined TP data with the interferometric images using the CASA task, feather. We used TCLEAN with Briggs’ robust weighting of 0.5 to the visibilities and an imaging option of MULTISCALE with scales of 0, 5, 15, 25, and 50 times the pixel size ($0''.2$), considering the spatially extended nature of the emission. We used the automasking algorithm, automultithresh (A. A. Kepley 2019), where the parameters of sidelobethreshold, noisethreshold, lownoisethreshold, negativethreshold, and minbeamfrac are set to 1.75, 2, 1.5, 0, and 0.3, respectively, mostly following the recommended values by (A. A. Kepley 2019).

The achieved beam size of HCO^+ , HNC and HC^{18}O^+ cubes are $(0.89\text{--}1.06)$ arcsec \times $(1.05\text{--}1.29)$ arcsec, whilst N_2H^+ cubes have beam size of $(1.10\text{--}1.38)$ arcsec \times $(1.40\text{--}1.80)$ arcsec. The velocity resolution of HNC, HCO^+ and HC^{18}O^+ is 0.27 km s $^{-1}$ and that of N_2H^+ is 0.19 km s $^{-1}$. Average 1σ rms noise level measured from line-free channel is ~ 7 and 5 mJy beam $^{-1}$, corresponding to 1.0 K and 0.3 K, for Band 6 and Band 3 cubes, respectively. All data shown in the paper about these three lines are ALMA 12 m, bf 7 m, and TP combined, and before the primary beam correction. Appendix B discusses how combining TP data with interferometric data affects the line shape.

Additionally, in this paper, we also use the 1.3 mm continuum emission and the optically thin tracers of DCO^+ ($J=3\text{--}2$), N_2D^+ ($J=3\text{--}2$), DCN ($J=3\text{--}2$) from the ASHES project (S. Li et al. 2022, 2023; K. Morii et al. 2023, 2024), see Appendix A. These are 12m+7m combined datasets without TP combination, but with a

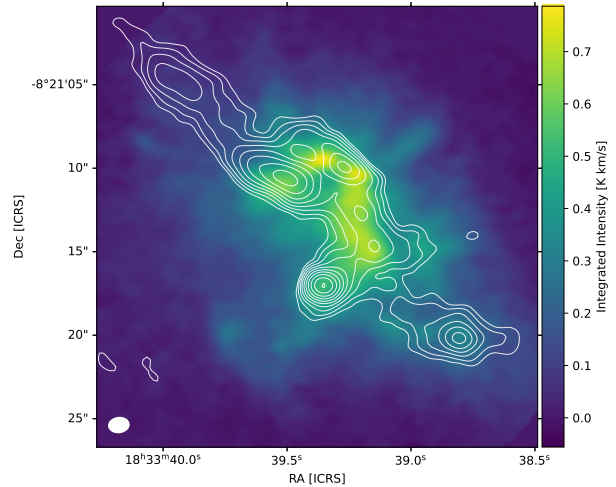


Figure 1. Moment 0 map of HNC overlaid with continuum emission as white contours. The beam size is shown in the bottom left corner. Contour levels are $5\sigma \times \sqrt{2}^n$ ($n=1,2,3,\dots$), where $1\sigma=0.1$ mJy beam $^{-1}$.

similar beam size of $\sim 1.2''$. Core physical information such as size, mass, density, virial parameter, and evolutionary stages has been taken from K. Morii et al. (2023) and K. Morii et al. (2024).

3. RESULTS

3.1. Spatial distribution

Figure 1 shows the integrated intensity (zeroth-order moment) map of HNC, overlaid with 1.3 mm dust continuum. It indicates the consistency between bright spots of HNC and dust continuum emission, as well as a more extended distribution of HNC emission than dust continuum.

Figure 2 shows (a) line spectra map of HNC overlaid on a three color image (r/b/g: CO redshifted, CO blue shifted, and continuum), and (c) zoom-in spectral map of HNC (green), HCO^+ (blue) and DCO^+ (orange) around the brightest core. It indicates that double peak profiles are seen widely spread in the field, not only around or inside dense cores but also in inter-core regions. Spectra that overlap with CO outflows sometimes have high-velocity or tail/wing components. Panel (b) shows the comparison of the spectra. HNC and HCO^+ show double peak profiles around the most massive core, where DCO^+ typically peaks at their dip velocity. The profiles of HNC and HCO^+ look generally the same, but sometimes differ in intensity and peak velocity, for example the profile at RA=18h33m39.40s and Decl.=−8d21m16s.

Table 1. Summary of ALMA Observations

Band	Config.	Obs. Dates	Baselines (m)	N_{ant}	Total time ^a (min)
Band 6	12m (C43-1, C43-2)	2024 Mar. 17–2024 Dec. 10	15.1–313.7	43–47	7–15
	7m	2024 Jan. 21–2024 Jun. 13	8.9–48.9	8–11	50–97
Band 3	12m (C43-3, C43-4)	2024 Jan. 15–2025 Jan. 25	15.1–783.5	35–46	13–22
	7m	2023 Oct. 25–2024 Jan. 26	8.9–48.9	7–10	29–58

^aOn-source integration time per region.

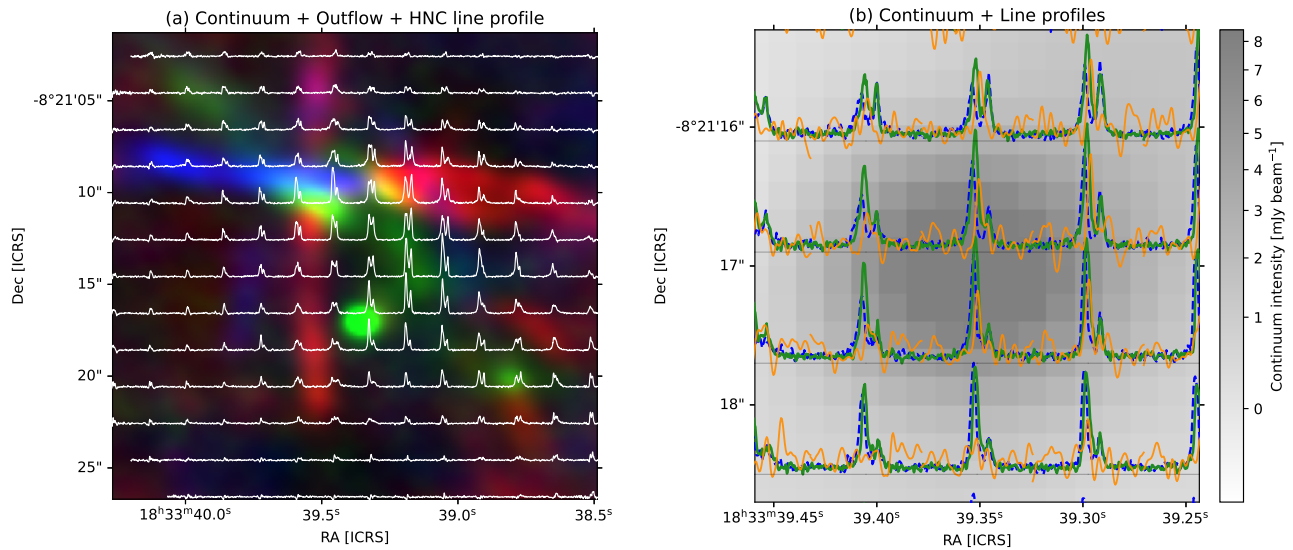


Figure 2. (a) HNC line-spectra map (binned to $10 \text{ pix} \times 10 \text{ pix}$) overlaid on a three-color composite image: CO outflow in red and blue, and continuum emission in green. (b) Line profiles of DCO^+ (orange), HCO^+ (blue dashed), and HNC (green) toward ALMA 1 (the brightest core), binned to $4 \text{ pix} \times 4 \text{ pix} \sim 1 \text{ beam}$. Gray-scale background is 1.3 mm continuum. Each spectrum is normalized by the brightest peak intensity.

3.2. Line Detection

Line profiles of HCO^+ and HNC toward the 304 identified cores were extracted by averaging within the cores. This was done by creating an ellipse mask from the major and minor axes and position angle information obtained from dendrogram analysis applied to continuum emission (K. Morii et al. 2023). HCO^+ emission was detected in 282 cores, and HNC in 285 cores, at the $> 5\sigma$ noise level. The detected profiles exhibit a variety of morphologies, including single peaks, skewed profiles, and double peaks with either the blue or red peak stronger. High-velocity line wings and tails indicative of outflows were also observed in a subset of cores, especially in HCO^+ . Figure 13 in Appendix C presents several examples of the extracted profiles.

Using the HC^{18}O^+ ($J = 3 - 2$) as an optically thin reference, we estimated the peak optical depth of HCO^+ ($J = 3 - 2$) for 30 cores in three representative regions

(see Appendix D for details). For cores where HC^{18}O^+ is detected, the derived optical depths ($\tau = 1.7 - 11.4$). These values serve as lower limits due to the uncertainties in excitation temperature, thereby confirming that the optically thick assumption is valid for these sources. For cores without HC^{18}O^+ detection, predominantly low-mass prestellar cores, only upper limits could be obtained. However, none of these upper limits indicate clearly optically thin conditions. Therefore, in the following analysis, we treat both HCO^+ and HNC as optically thick tracers.

3.3. Infall Statistics

Blue asymmetry profiles sometimes refer to both blue skew profiles and double peak profiles with the blue peak stronger (or blue double peak profile). To avoid contamination from the multi-velocity components in a line of sight, the blue asymmetry profile is confirmed with an

optically thin line. If the optically thick line shows a double peak profile with a dip close to the systemic velocity, where an optically thin line shows a single peak, the profile is considered to be an indicator of inward or outward motion. If the blue-shifted component is brighter, it implies inward motion. A profile without a clear dip but with a blue skew, indicating that the peak is shifted to the blue side relative to the systemic velocity, is defined as a blue-skew profile. After determining the systemic velocity for all the cores (see Appendix A), we employed two methods to quantitatively characterize blue asymmetry profiles:

1. Velocity Difference by D. Mardones et al. (1997):

$$\delta_v \equiv \frac{V_{\text{thick}} - V_{\text{thin}}}{\Delta V_{\text{thin}}} \quad (1)$$

Here V_{thick} is the brightest peak velocity of the optically thick line, V_{thin} is the peak velocity of the optically thin line tracing the systemic velocity of the dense core, and ΔV_{thin} is the full width at half maximum (FWHM) of the optically thin line. The blue asymmetries correspond to $\delta_v < 0$. Restrictively, $\delta_v < -0.25$ is considered to be a significant blue asymmetric profile.

2. Asymmetry Parameter by J. M. Jackson et al. (2019):

$$A \equiv \frac{I_{\text{blue}} - I_{\text{red}}}{I_{\text{blue}} + I_{\text{red}}}, \quad (2)$$

where I_{blue} is the integrated intensity at velocities less than the reference velocity and I_{red} is the integrated intensity at more positive velocities. The integration range for I_{blue} extended from $V_{\text{thin}} - 2\Delta V_{\text{thin}}$ to V_{thin} and that for I_{red} was from V_{thin} to $V_{\text{thin}} + 2\Delta V_{\text{thin}}$, where V_{thin} is the reference line velocity and ΔV_{thin} is the observed velocity FWHM of optically thin line. A represents the fraction of the total line flux that lies to the blueshifted (or redshifted) side of the systemic velocity. In this scheme, line profiles with a blue asymmetry will have values of $A > 0$, symmetric line profiles will have $A = 0$, and line profiles with a red asymmetry will have $A < 0$. Larger absolute values of A are more asymmetric line profile. In the absence of absorption against a continuum source, A is bounded between -1 and +1.

Applying these methods to both HCO^+ and HNC, we found almost consistent results across the two metrics and also across the lines. Figure 3 shows the δ_v and A scatter plots derived for both HCO^+ (blue) and HNC (green). Cores with a large uncertainty ($>100\%$)

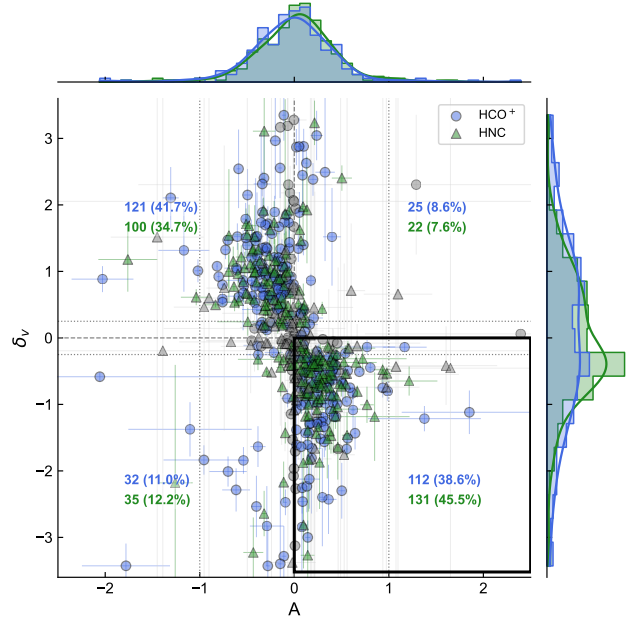


Figure 3. δ_v and A scatter plots derived by HCO^+ (blue) and HNC line (green). Cores with large uncertainties ($>100\%$) are colored gray. The histogram and Kernel Density Estimation (KDE) plots for each parameter are shown on the right and top, respectively. The percentage of data points in each quadrant is denoted as colored text. The quadrant enclosed by a thick black line corresponds to the blue asymmetry in both parameters. Cores with a clear single peak detected either DCO^+ or N_2D^+ have black edge circles. Faint dotted lines mark $A = \pm 1$, beyond which ($|A| > 1$) absorption is implied by definition, and $\delta_v \pm 0.25$, the adopted velocity threshold (see main text).

are colored in gray. The uncertainties for both parameters are estimated following J. M. Jackson et al. (2019). The majority of the sample lies along the line from the top-left to the bottom-right, implying consistent classification from the δ_v and A parameters. Quantitatively, in terms of δ_v , 50.3% and 58.0% of cores have $\delta_v < 0$, corresponding to inward motion, in HCO^+ and HNC, respectively. More restrictively, $\delta_v < -0.25$ are found in 40% and 45% of the whole sample. In terms of A , 48.3% and 53.7% of cores show $A > 0$ in HCO^+ and HNC, respectively. Some cores show $|A| > 1$ due to absorption in the profile. Compared to HCO^+ , a higher percentage of inward-indicating results is obtained from HNC lines. This is clearly seen in the histogram of δ_v , whose peak is located < -0.25 . However, the fraction of blue asymmetry profiles is still not significantly higher than that of red asymmetry.

3.4. Line Profile

Beyond the quantitative asymmetry measures, we further characterize the profile by its shape. As discussed in

Appendix B, ignoring TP data may cause significantly different results in such analysis. We measured the peak velocity and performed one- or two-Gaussian fits, and using the velocity dispersion (σ) and peak velocity separation ($\Delta V = |v_{\text{gauss},1} - v_{\text{gauss},2}|$), we classified spectrum into single, skew, double peak, or complex classes as summarized in Figure 4. The detailed steps are described in Appendix C.

As a result, $\sim 60\%$ of the sample is classified as double peak profiles by both HCO^+ and HNC , which can be roughly described by two Gaussians. 15% show a skew profile without a clear dip or profile described by a closely located two Gaussians, 10% show a single peak, and the other $\sim 15\%$ show a complex profile. Some examples of the classification are shown in Figure 13. Figure 14 in the Appendix shows the correlation plot of line classification between HCO^+ and HNC , indicating the good correlation between the two lines, albeit with occasional discrepancies in classification. More detailed discussion of these classifications and cores' physical properties is presented in Section 4.2. All the measured parameters and classifications are listed in Table 2.

How such classification correlates with δ_v and A parameters can be confirmed in Figure 5, where color represents the classification. Cores showing double peak profiles (dark orange and navy colors) have larger $|\delta_v|$ and $|A|$, while skew peak profiles (orange and blue) are found in cores showing smaller absolute values. Single profiles (green) are seen around 0 in both parameters. These results confirm that the quantitative asymmetry parameters and the morphological classification are in good agreement.

4. DISCUSSION

4.1. Infall Statistics and Cores Properties

As they deviate from zero, both A and δ_v indicate stronger inward/outward motion. Figure 6 shows the δ_v and A scatter plots colored by cores' evolutionary stages. The left and right panels show HCO^+ and HNC , respectively. The cores' evolutionary stages are classified in K. Morii et al. (2024). Cores associated with outflows (red diamonds) and with the detections of warm gas tracers (green crosses) are protostellar core candidates. Prestellar core candidates without any signs of protostars are plotted as blue squares.

The difference among the evolutionary stages in the A parameter lies in its dispersion, with prestellar cores showing greater variation. The median value does not differ significantly among the three evolutionary stages, but A estimated from HNC peaks at $A > 0$. Similarly, the δ_v distributions for all evolutionary stages take a peak $\delta_v < -0.25$ in HNC , indicating the large population

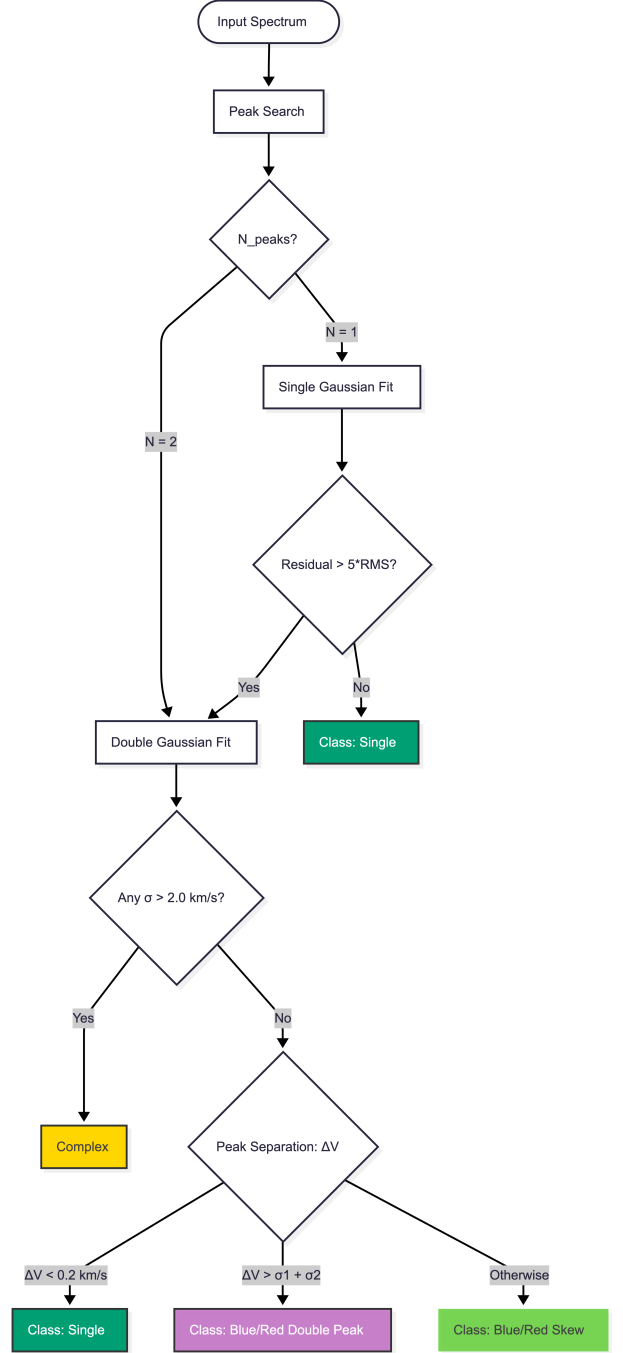


Figure 4. Decision tree for line profile classification. The algorithm determines the spectral class by sequentially evaluating the number of peaks, Gaussian fit results (σ and ΔV). Classes are color-coded: green for Single, purple for Double Peak, light green for Skew, and yellow for Complex.

showing inward motion in HNC . In δ_v , a bimodal distribution is seen in protostellar cores, although prestellar cores show relatively smaller $|\delta_v|$ values with a single peak. The median value or the peak of δ_v distribution shifts to smaller values as evolution, implying that

Table 2. Summary of Infall Parameters^{*}

Region	ID	Evolutionary Stage ^a	Gravitational Boundness ^b	V_{cen} (km s^{-1})	σ_{thin} (km s^{-1})	δ		A		Spectral Class	
						HCO ⁺	HNC	HCO ⁺	HNC	HCO ⁺	HNC
G016.97	1	outflow	bound	41.34	0.36	-0.90	-0.57	0.41	0.40	blue double peak	blue double peak
G016.97	2	warm	bound	40.54	0.26	0.30	0.31	0.20	0.11	red skew	red skew
G016.97	3	prestellar	bound	40.67	0.31	-0.31	-0.30	0.16	0.02	blue double peak	blue skew
G016.97	4	prestellar	non-detection	40.41	0.34	-0.30	-0.28	0.41	0.21	blue skew	blue skew
G016.97	5	outflow	non-detection	41.32	0.40	-1.08	-1.64	0.62	0.46	blue double peak	blue double peak
G016.97	6	prestellar	non-detection	40.35	0.37	-0.98	-0.19	0.33	0.13	complex	blue skew
G016.97	8	prestellar	non-detection	40.47	0.29	2.18	-0.42	-0.04	-0.07	red double peak	blue double peak
G016.97	9	outflow	non-detection	40.46	0.14	-0.06	-0.42	0.41	1.61	single	single
G016.97	10	prestellar	non-detection	40.52	0.37	0.22	0.54	-0.01	-0.31	red skew	red skew
G016.97	11	prestellar	non-detection	40.88	0.45	0.63	-0.27	-0.45	-0.01	red double peak	blue double peak

^{*} Full version is available online as machine-readable table.

^a Determined based on the detections of CO outflow and warm gas tracers in S. Li et al. (2022) and K. Morii et al. (2024).

^b Determined from the virial analysis considering gravity and non-thermal velocity dispersion excluding external pressure and magnetic field support (K. Morii et al. 2024).

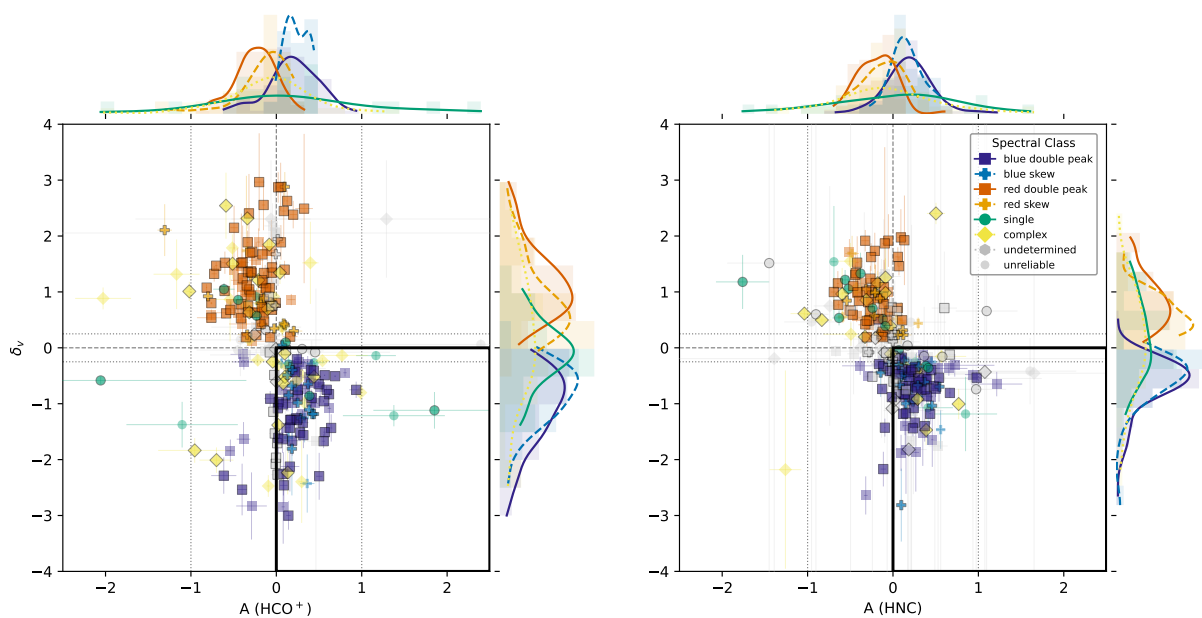


Figure 5. δ_v and A scatter plots colored by classified categories. Solid and dashed KDE curves represent double-peak and skewed spectral profiles, respectively. As with Figure 3, a black edge means the core has a clear single peak in DCO^+ or N_2D^+ , while others have multiple peaks or no detections of DCO^+ nor N_2D^+ . Cores with large uncertainties ($>100\%$) are colored gray.

inward motion is more clearly seen in the protostellar phase. Since protostellar cores are more massive and denser (K. Morii et al. 2026), there is a weak correlation indicating that more massive and denser cores show relatively smaller δ_v and larger A , which is discussed in Appendix E.

4.2. Line Profile Classification and Core Properties

Figure 7 shows the core physical properties distribution (M , Σ , α_{vir}) along with the spectral classification. The left and right columns show the case of HCO⁺ and HNC, respectively. Overall, the features seen in these plots are independent of the lines. Single and red skew profiles are seen in cores with low-mass, low-density, and relatively high virial parameters. Blue skew, blue double-peak, and red double-peak profiles are found in relatively more massive and dense cores with a small virial parameter ($\lesssim 2$). Complex profiles are also found in low- to high-mass cores.

Figure 8 shows the percentage of each profile by dividing the sample into several mass and surface density bins in the first two rows. It clearly shows that the percentage of single-peak profiles decreases, while the percentage of blue double-peak profiles generally increases as mass and density increase. Considering HCO⁺ is more affected by outflows and focusing on the HNC plots, the blue asymmetry profile is the dominant category at the highest mass and density bin.

It should be noted that, considering the physics behind the double peak profile, it is natural to see a clearer double peak profile in denser and more massive objects, where there is likely a steeper density and temperature gradient. Single or skew profiles in low-mass, low-density cores imply that those conditions may not be sufficient to make 3-2 lines optically thick (see also Section 3.2). However, as mentioned in the previous search for suitable lines tracing infall by numerical simulation (e.g., R.-A. Chira et al. 2014; J.-J. Xie et al. 2021), lower transitions would suffer more from the ambient gas around cores, raising the complexity to observe inward motion from low-mass, lower-density cores in massive clumps.

The line profile classification and the relation with cores' evolutionary stage are summarized in the third row of Figure 8. Prestellar cores have the highest percentage of skew and single profiles. On the contrary, outflow-associated cores tend to show a double-peak profile (70% when combining blue and red cases), indicating a broader line width. This implies that the blue asymmetry profile emerges from the prestellar stage and becomes increasingly dominant as evolution proceeds.

Interestingly, we detected clear blue asymmetry profiles even in cores classified as gravitationally unbound (virial parameter $\alpha_{vir} > 2$). The bottom row of Figure 8 shows the percentage for each category. Although the percentage ($\sim 20\%$) is not as high as bound cores ($\sim 30\text{--}40\%$), this is also confirmed in the scatter plot (right column of Figure 3) where some unbound cores ($\alpha_{vir} \sim 2\text{--}4$) show $A > 0$ and $\delta < 0$. This finding may challenge the simple interpretation of virial analysis, where external pressure is not considered. Or, as implied by K. Morii et al. (2025), this may be due to the overestimation of the non-thermal velocity dispersion caused by the broadening produced by local infall motions. It suggests that these cores may be undergoing collapse driven by external pressure (e.g., from the surrounding clump weight or feedback), rather than purely by self-gravity, as expected in accretion-driven star formation (G. C. Gómez et al. 2021), or turbulent fragmentation (K. Ishihara et al. 2025).

Our statistical analysis reveals that blue asymmetry is detected in nearly 60% of the dense cores, excluding complex profiles. Numerical simulations by R. J. Smith et al. (2012, 2013) suggest that viewing angles, complex filamentary geometries, and large-scale gas flows can easily obscure infall signatures even in genuinely collapsing cores. The measured fraction is comparable to that reported by R.-A. Chira et al. (2014) for collapsing objects in simulations without feedback, implying that core-scale collapse is prevalent in 70 μm -dark clumps. The fact that blue asymmetry is not ubiquitous likely reflects the combined effects of unfavorable viewing geometry and outflow contamination, rather than an absence of infall.

4.3. Hierarchical Inward Motion

Gravitational collapse occurs not only at the core-scale but also at the clump-scale. Using the total-power data, we measured δ_v and A parameters at the clump-scale. The measured parameters are listed in Table 3. Figure 9 is the same plot as Figure 3, but for clump-scale profiles. The overall trend, such as the correlation between two parameters, is similar; however, the parameter space is much smaller. For example $|\delta_v| < 0.6$ for clumps, but $\lesssim 2$ for cores. Compared to core-scale, clump-scale HCO⁺ and HNC profiles are more likely to show a single peak, especially for HNC, resulting in small δ_v and A variation. In clump-scale, HCO⁺ rather shows blue-skew or double-peak profiles. This is consistent with J. M. Jackson et al. (2026), who report that HNC and HCN tend to show smaller asymmetries than HCO⁺ due to their lower optical depth. Even at core scales, HNC becomes optically thick closer to the core center than HCO⁺ (R.-

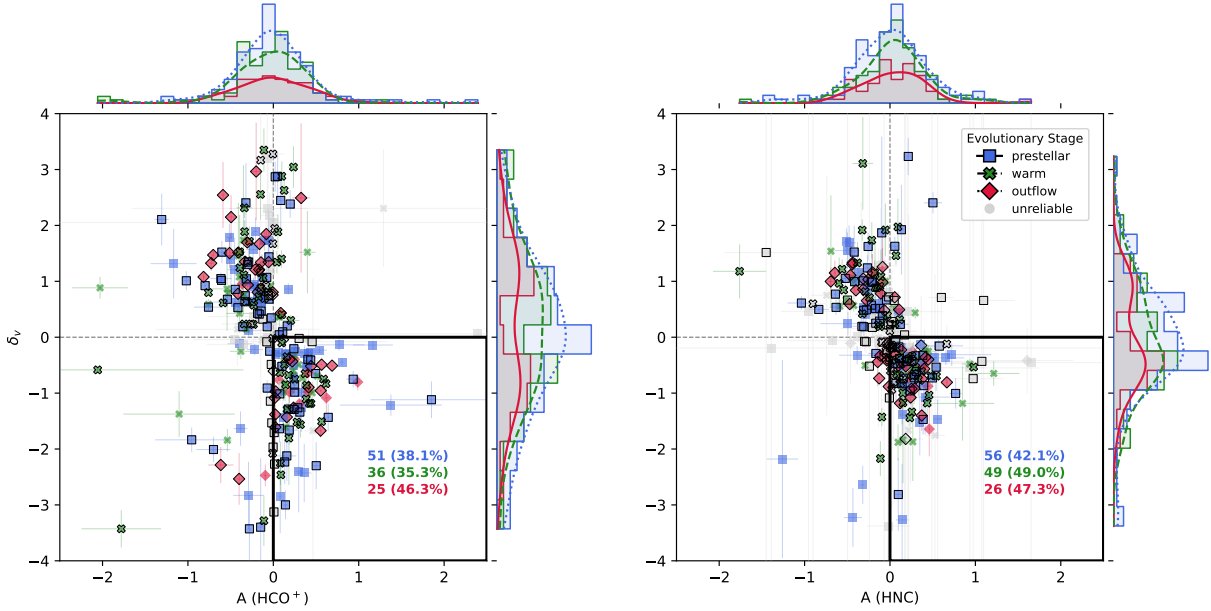


Figure 6. δ_v and A scatter plots colored by cores’ evolutionary stages. As with Figure 3, a black edge means the core has a clear single peak in DCO^+ or N_2D^+ . Cores with large uncertainties ($>100\%$) are colored gray.

A. Chira et al. 2014), so based on optical depth alone, HCO^+ would be expected to show a higher blue asymmetry fraction. The fact that the opposite trend is observed, though not significantly, is consistent with the earlier finding that HCO^+ profiles are more affected by outflows and diffuse gas flows, which can suppress or distort infall signatures.

We investigate the preferred physical conditions for detecting blue asymmetry profiles at the clump scale and their correlation with core-scale inward motion. We find some moderate correlation with clump density, protostellar core fraction and number of cores, which roughly traces the evolution of clumps. The left three panels of Figure 10 are scatter plots of A and δ derived from HCO^+ with clump density, protostellar core fraction, and the number of cores. Data implying inward/outward motion are colored by blue and red, respectively. There is a moderate correlation, implying the clearer inward motion is seen in denser, likely more evolved clumps, with a larger number of cores.

The two right panels of Figure 10 show the correlation found between clump-scale A and δ derived from HCO^+ and core-scale profile classification. $f_{blue,all}$ is the fraction of blue-skew or blue-double peak profiles against the total number of cores in the region. All values used for the plots are in Table 3. The correlation between clump-scale and core-scale inward motion implies multiscale, hierarchical collapse (e.g., R. J. Smith et al. 2009; E. Vázquez-Semadeni et al. 2024): if clumps show inward motion, a higher percentage of cores show

inward motion. However, we cannot fully rule out the possibility that the TP data partially reflect the cumulative emission from multiple cores rather than purely tracing the diffuse clump gas. Lower-transition observations would help to disentangle these contributions.

4.4. Implications for Infall Velocity

Before applying an infall model, we obtain a rough idea of the infall velocity and its variation with the peak difference or the peak velocity offset from the dip velocity. Figure 11 shows the difference of $v_{dip} - v_{sys}$ and the velocity difference of the two peaks ΔV_{peak} if available, which roughly trace the infall velocity and the velocity dispersion, respectively. The top row indicates a weak trend of higher infall velocity with increasing evolution or mass. The median value is almost flat in both HCO^+ and HNC plots. This implies a weak correlation between the evolutionary stage of cores and the expected infall velocity. The bottom row indicates an increase in velocity peak separation, implying a broader line width or stronger turbulence with evolution. However, as suggested by C. H. De Vries & P. C. Myers (2005), for example, more careful fitting with parameters of optical depth, temperature, and density, as well as infall velocity, is required to estimate the infall parameters.

5. CONCLUSIONS

We have presented the first large-scale statistical survey of gravitational infall signatures in high-mass dense cores using ALMA observations of optically thick molecular lines HCO^+ ($J=3-2$) and HNC ($J=3-2$). Our anal-

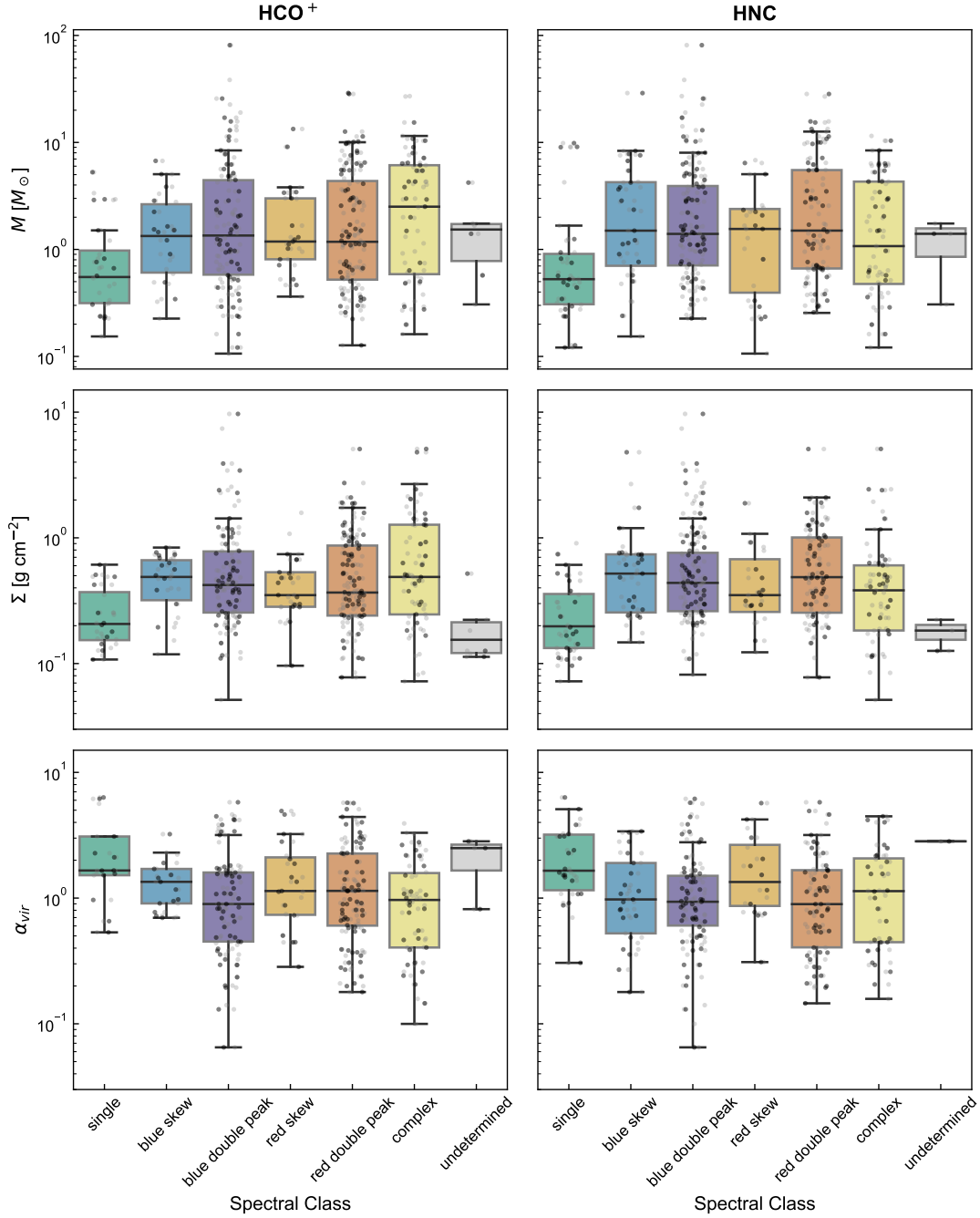


Figure 7. Core physical parameters' variation against the spectral classification. The box plots show the 0th, 25th, 50th, 75th, and 100th percentiles, with outliers plotted individually. Cores with a single clear peak in DCO^+ or N_2D^+ are colored in black, while others are gray.

ysis of 304 dense cores within 24 massive $70 \mu\text{m}$ -dark clumps from the GLASHES survey provides comprehensive evidence that core-scale collapse is prevalent in the earliest stages of high-mass star formation. The main findings of this study are summarized as follows:

1. Blue-asymmetric line profiles, indicative of infalling gas motions, are detected in approximately 50–60% of the cores using both the velocity dif-

ference parameter ($\delta_v < 0$) and the asymmetry parameter ($A > 0$). More restrictive criteria ($\delta_v < -0.25$) yield detection rates of 40–45%. Spatially, these profiles are found not only inside cores but also around cores. Considering that geometric effects and viewing angles can obscure infall signatures in genuinely collapsing cores, our re-

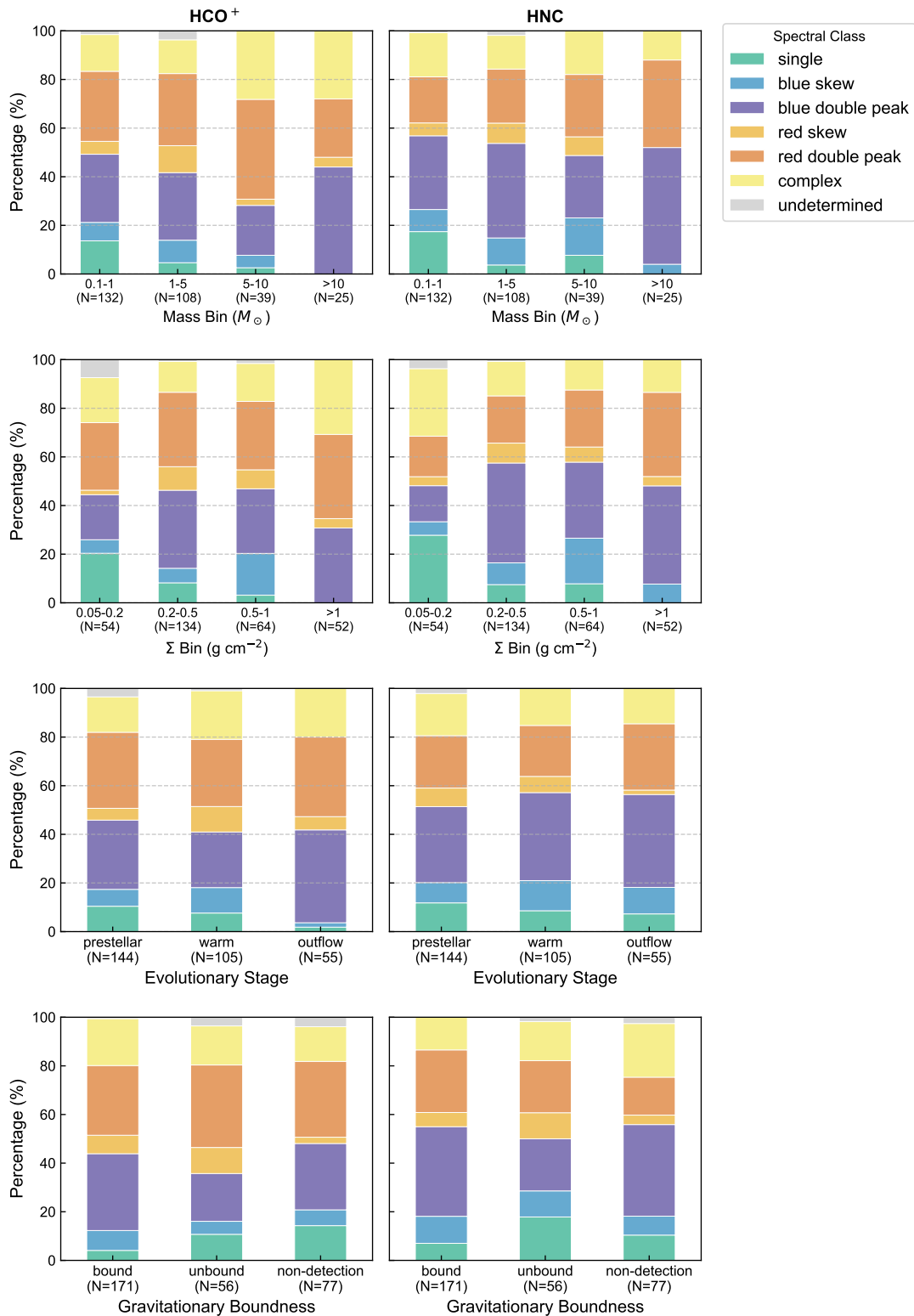


Figure 8. The percentage of the spectral classes against the core mass, the surface density, the evolutionary stages, and gravitational boundness.

Table 3. Summary of Clump Properties

Region	$n(\text{H}_2)^a$	f_{proto}^b	N_{core}^c	$f_{\text{blue,all}}$		A_{cl}	δ_{cl}
	10^4 cm^{-3}			HCO^+	HNC		
G016.97	4.19	0.38	12	0.33	0.33	0.14	-0.28
G018.80	4.09	0.75	6	0.17	0.17	-0.07	0.37
G018.93	2.04	0.47	5	0.20	0.20	-0.31	0.55
G022.69	1.75	0.42	9	0.11	0.11	-0.25	0.07
G023.47	8.39	0.53	12	0.75	0.75	-0.00	-0.11
G024.01	11.52	0.62	13	0.46	0.46	0.17	-0.62
G024.52	2.91	0.65	18	0.33	0.33	0.43	-0.38
G025.16	3.74	0.56	13	0.46	0.46	0.15	-0.48
G028.54	2.86	0.39	16	0.25	0.25	0.12	0.04
G028.56	8.36	0.71	26	0.23	0.23	0.03	-0.03
G028.92	2.44	0.56	7	0.57	0.57	0.15	0.06
G030.70	1.73	0.52	10	0.60	0.60	0.03	0.08
G030.91	6.17	0.42	10	0.50	0.50	0.08	0.08
G033.33	1.21	0.33	7	0.29	0.29	-0.35	0.37
G034.13	1.58	0.13	10	0.00	0.00	0.36	-0.08
G034.73	4.48	0.58	10	0.00	0.00	-0.01	0.29
G036.66	5.04	0.54	9	0.44	0.44	0.21	-0.20
G305.79	9.30	0.47	27	0.41	0.41	-0.06	0.10
G327.11	4.10	0.19	11	0.09	0.09	-0.09	0.35
G332.96	1.94	0.10	7	0.14	0.14	-0.07	0.32
G333.48	4.04	0.20	18	0.67	0.67	-0.05	-0.06
G333.52	10.93	0.71	28	0.43	0.43	0.36	-0.33
G337.54	5.64	0.53	11	0.18	0.18	-0.23	-0.17
G340.39	2.90	0.10	9	0.44	0.44	0.35	-0.19

^aEstimated in *K. Morii et al. (2023)*.

^bFraction of the protostellar cores estimated in *K. Morii et al. (2024)*.

^cNumber of cores in the field-of-views of GLASES observations.

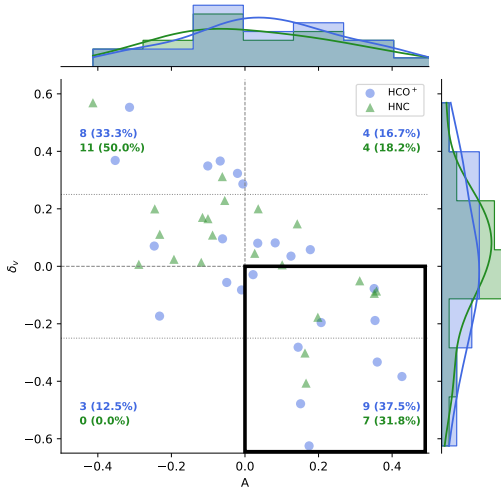


Figure 9. δ_v and A scatter plots derived by HCO^+ (blue) and HNC line (green) for each clump. Figure style is the same with Figure 3.

- sults imply that infall motion is occurring around a substantial fraction of cores.
- The two optically thick tracers yield broadly consistent results, with HNC showing slightly higher detection rates of blue asymmetry (58% vs. 50% for $\delta_v < 0$). This difference may reflect the fact that HCO^+ is more susceptible to contamination from outflow emission, which can introduce red-shifted components. Despite these minor discrepancies, the overall agreement between the two tracers strengthens the robustness of our infall classifications.
 - Approximately 60% of the sample exhibits double-peaked profiles that can be described by two-component Gaussian fits, while 15% show blue- or red-skewed profiles, 10% show single peaks, and the remaining $\sim 15\%$ display complex morphologies. Blue-asymmetric profiles become increasingly prevalent in more massive and denser cores, especially in cores with masses $M \gtrsim 10 M_\odot$ and surface densities $\Sigma \gtrsim 0.1 \text{ g cm}^{-2}$.
 - Blue asymmetry is detected across all evolutionary stages, from prestellar cores to protostellar cores associated with outflows and warm gas emission lines. As cores evolve, the profiles transition toward more pronounced double-peaked morphologies with larger velocity dispersions, suggesting increasing turbulence, feedback effects, or infall velocity. The shift in the median δ_v toward more negative values with evolutionary stage indicates

that infall signatures become more prominent in the protostellar phase.

- Remarkably, blue-asymmetric profiles are detected in $\sim 20\%$ of cores with virial parameters $\alpha_{\text{vir}} > 2$, which are nominally gravitationally unbound. This finding implies that external compression from the surrounding core material may trigger collapse, or non-thermal velocity dispersion is overestimated due to the contribution of infall motion.
- Analysis of clump-scale profiles reveals that inward motions occur simultaneously at both clump and core scales. We find a moderate positive correlation between clump-scale infall signatures and the fraction of cores showing blue asymmetry within those clumps. Clumps with higher densities, larger numbers of cores, and higher protostellar core fractions exhibit stronger infall signatures at both scales. This hierarchical pattern supports the clump-fed accretion scenario.
- Preliminary estimates based on dip velocities and peak separations imply a weak trend of increasing infall velocity and velocity dispersion with evolutionary stage and core mass.

In summary, our statistical survey demonstrates that gravitational collapse at the core scale is a prevalent and continuous process in high-mass star-forming regions. The detection of blue asymmetry across evolutionary stages, the infall signatures in nominally unbound cores, and the evidence for hierarchical inward motions from clump to core scales all underscore the dynamic and multi-scale nature of high-mass star formation.

ACKNOWLEDGMENTS

We thank the anonymous referee for their careful reading and constructive comments, which improved the manuscript. PS was partially supported by a Grant-in-Aid for Scientific Research (KAKENHI Number JP23H01221) of JSPS. This paper makes use of the following ALMA data: ADS/JAO.ALMA#2018.1.00299.S (PI: Y. Contreras), ADS/JAO.ALMA#2023.1.01150.S (PI: K. Morii) and ADS/JAO.ALMA#2024.1.01505.S (PI: K. Morii). ALMA is a partnership of ESO (representing its member states), NSF (USA) and NINS (Japan), together with NRC (Canada), NSTC and ASIAA (Taiwan), and KASI (Republic of Korea), in cooperation with the Republic of Chile. The Joint ALMA Observatory is operated by ESO, AUI/NRAO

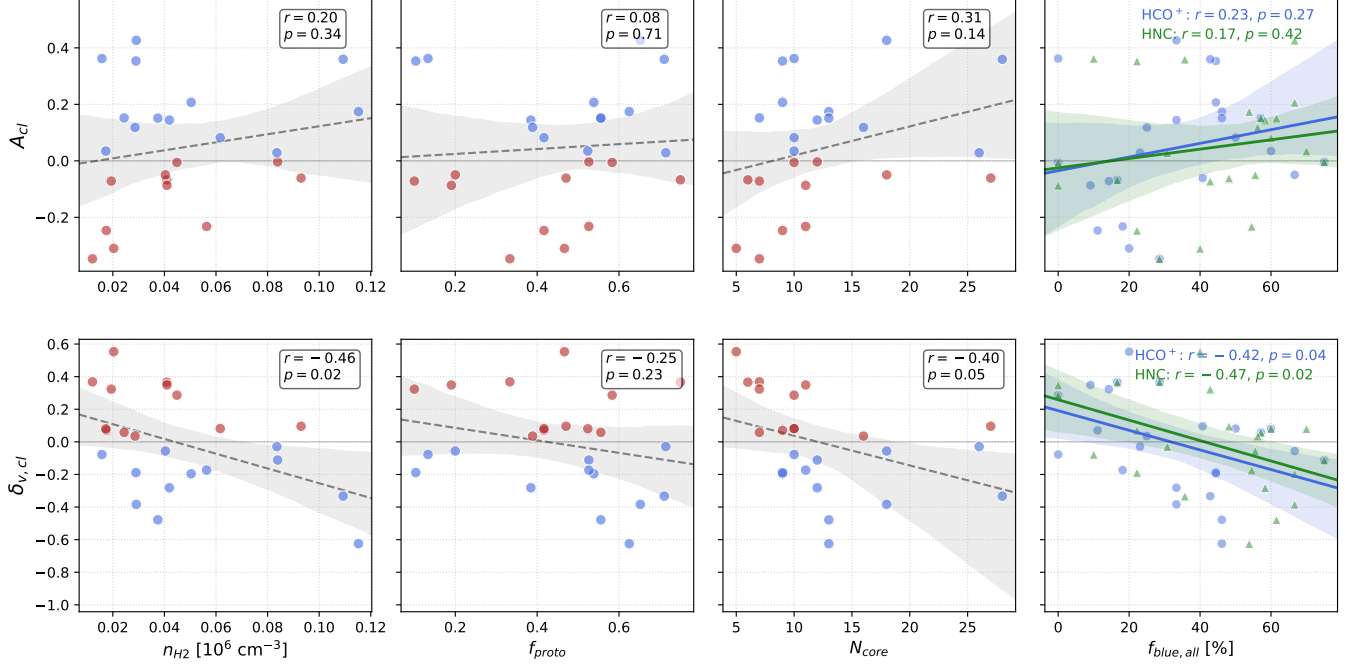


Figure 10. Scatter plots of the clump-scale A_{cl} and $\delta_{v,cl}$ derived from HCO⁺ line against the clump volume density (n_{H_2}), the protostellar core fraction, number of cores, and the fraction of cores showing blue asymmetric profiles ($f_{blue,all}$). Colors in the left three panels indicate whether the estimated A_{cl} or $\delta_{v,cl}$ imply blue or red asymmetric profiles. The color in the right panel represents the species used for estimating $f_{blue,all}$. Regression plots are overlaid. Pearson correlation coefficients are denoted on the top-right.

and NAOJ. The National Radio Astronomy Observatory is a facility of the National Science Foundation operated under cooperative agreement by Associated Universities, Inc.

Software: Astropy (Astropy Collaboration et al. 2013, 2018, 2022), CASA (CASA Team et al. 2022), Matplotlib (J. D. Hunter 2007), Numpy (C. R. Harris et al. 2020), seaborn (M. L. Waskom 2021).

Facility: ALMA

APPENDIX

A. SYSTEMIC VELOCITY DETERMINATION

To determine the systemic velocities (V_{thin}) of the 304 cores in our sample, we first utilized the optically thin DCO⁺ and N₂D⁺ ($J=3-2$) lines. K. Morii et al. (2024) applied a single Gaussian fit to the core-averaged spectra and estimated the properties for 227 cores. We excluded 5 cores from this subset due to marginal 3σ detections and ambiguous systemic velocities, leaving 222 cores with robust DCO⁺ or N₂D⁺ measurements.

By carefully checking the spectra of these 222 cores, along with DCN ($J=3-2$), we found that 39 cores host multiple velocity peaks. In particular, clumps G025.16, G028.56, G305.79, G333.48, G333.52, and G340.39 contain more than three cores showing multiple components. For these 39 cores, we determined the representative velocity from the brightest DCO⁺ peak and added a flag to distinguish them from those with a single velocity component.

For the remaining 82 cores (i.e., 304 total – 222) where neither DCO⁺ nor N₂D⁺ was securely detected, we fit an isolated hyperfine component of N₂H⁺ ($J=1-0$, $F_1, F = 0, 1-1, 2$, $\nu = 93.176265$ GHz). Through this method, we obtained V_{thin} for 68 of the 82 cores. Consequently, we successfully derived velocity information from optically thin lines for a total of 290 cores (222 from DCO⁺ or N₂D⁺ + 68 from N₂H⁺). For the final 14 cores without any thin line detections, we assigned the average V_{thin} of their respective regions.

To reduce the impact of ambiguous V_{thin} measurements in our analysis, we flagged a total of 121 cores: the 82 cores lacking DCO⁺ or N₂D⁺ detections and the 39 cores exhibiting multiple components. This leaves a highly reliable

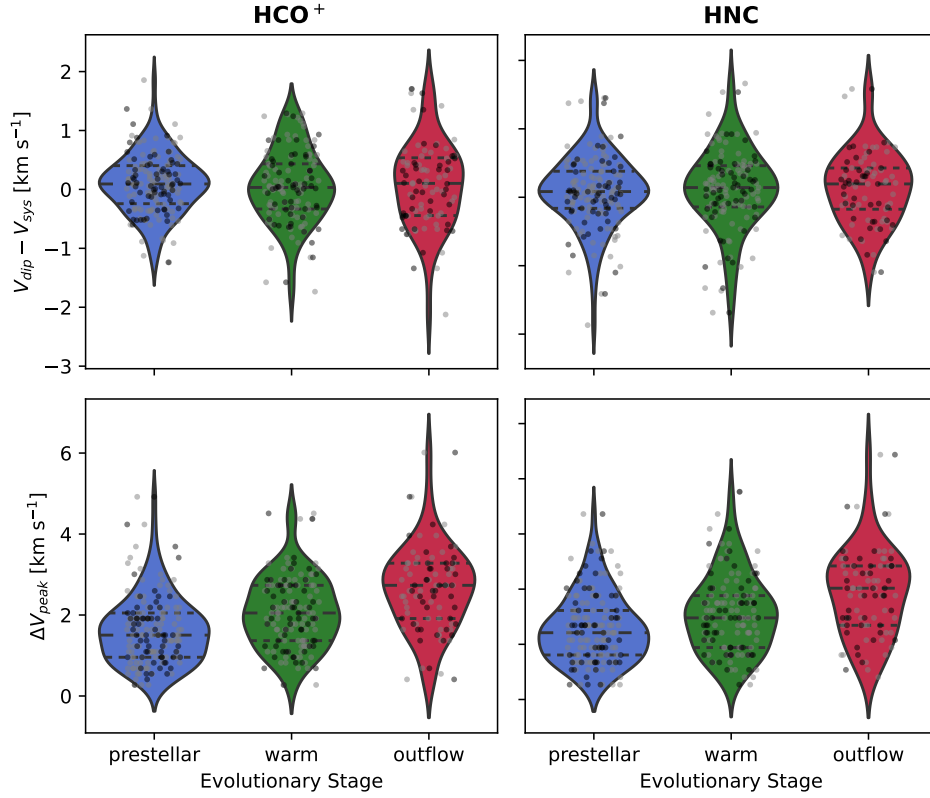


Figure 11. Distributions of dip velocity offset and peak separation across evolutionary stages. Top panels show the velocity difference between the absorption-like dip and the systemic velocity ($V_{\text{dip}} - V_{\text{sys}}$), serving as a proxy for infall velocity. Bottom panels show the velocity separation between the two peaks (ΔV_{peak}), reflecting the line width and internal turbulence. The samples are categorized into three evolutionary stages: prestellar (blue), warm (green), and outflow-associated (red) cores. Individual core data points are overlaid on each violin plot.

sub-sample of 183 cores. The 121 flagged cores are highlighted in most of the figures. The derived V_{thin} for each core is summarized in Table 2.

B. TOTAL-POWER DATA COMBINATION EFFECTS

In our data analysis, we combine total power data to recover the extended emission lost due to the interferometer. To illustrate the significance of this process, in this Appendix we compare the data before and after the TP combination. Figure 12 shows the difference in the spatial distribution and profile of the emission. From left to right, the images show a single channel of a 12-m data cube, a 12-m + 7-m combined data cube, and a 12-m + 7-m + TP combined data cube, respectively. The color scale of the three images is the same. Clearly, the peak intensity and spatial distribution differ. Panel (a) shows negative components around the continuum cores, while panel (c) shows more extended emission than the continuum. The spectrum in panel (d) also clearly illustrates the differences. There is no significant difference far from the line center ($v_{\text{l sr}} \sim 88 \text{ km s}^{-1}$), however, differences in intensity of a factor of a few exist around $v_{\text{l sr}} \sim 85.5\text{--}90 \text{ km s}^{-1}$. Regardless of the infall profile classification or modeling based on the line profile, it is clear that the combination of the 7 m and TP matters and can alter the conclusion.

C. LINE PROFILE CLASSIFICATION

The spectral profile was classified using a combination of peak-based criteria, dip significance, and Gaussian decomposition parameters. First, all local intensity maxima with $S/N > 3$ were identified within a velocity range of $\pm 4 \times \sigma_{\text{thin}}$ around the systemic velocity (V_{sys}). A peak was considered significant only if its amplitude exceeded the rms noise level by a factor of 3. The significant peaks were then divided into blue-shifted and red-shifted groups. If no reliable peak velocity could be determined, the profile was labeled as *undetermined*. When multiple significant peaks

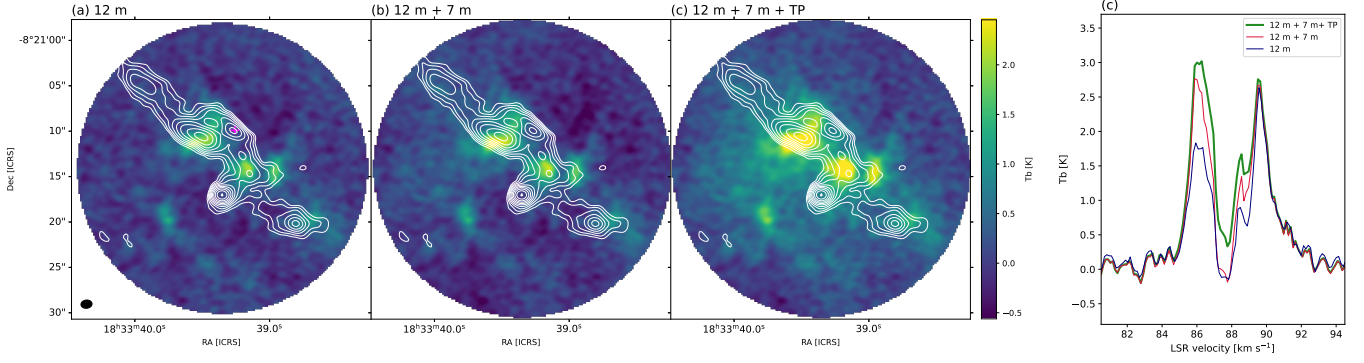


Figure 12. Comparison of the spatial distribution of the emission and the line spectra with and without Total Power data. The left three images are one slice of the cube at the same channel and color level, but (a) 12 m-only, (b) 12 m + 7 m, and (c) 12 m + 7 m + TP, respectively. The line spectra on panel (d) show the direct comparison of the spectra at the pixel where the magenta cross is in panel (a). Green, red, and navy lines represent the different cases of the data combination. White contours are the same with Figure 1.

were present on either side, we selected only the strongest peak (i.e., the peak with the maximum intensity) as the representative blue or red component.

For profiles with $N_{\text{peak}} = 2$ (i.e., both blue and red peaks exist), a double-Gaussian model was applied immediately. For other cases, a single-Gaussian fit was first performed. If the resulting residuals exceeded $5\sigma_{\text{rms}}$ noise level, the model was upgraded to a double-Gaussian to account for hidden sub-structures. When a two-component Gaussian fit was available (six fit parameters), for each fitted Gaussian, the observed peak velocities close to each centroid velocity were identified. The relative amplitudes at these matched peak velocities were then compared to determine whether the dominant component lies on the blue- or red-shifted side relative to the systemic velocity. This matching procedure is necessary because extended components, such as outflows, can produce broad Gaussian fits whose centroids are displaced from the local spectral maxima.

Then, the velocity separation between the two Gaussian centroids (Δv) and the sum of their widths $\sigma_1 + \sigma_2$ were used to distinguish morphological types:

- If $\Delta v < 0.2 \text{ km s}^{-1}$, the profile was classified as *single*.
- If $\Delta v > \sigma_1 + \sigma_2$, the profile was classified as a *double peak*; the dominant side (blue or red) was indicated according to the matched amplitudes.
- Otherwise, the profile was classified as *blue-skewed* or *red-skewed* depending on which side exhibited the stronger matched component.
- If either Gaussian width satisfied $\sigma > 2.0 \text{ km s}^{-1}$, the profile was labeled as *complex*.

When only a single-Gaussian fit was available, the profile was classified as *single*. If Gaussian fitting was not available or not conclusive, classification was done based on the peak velocity information: two detected peaks with separation $< 0.2 \text{ km s}^{-1}$ were labeled *single*; peaks separated by $> 2.0 \text{ km s}^{-1}$ were labeled *complex*; intermediate separations were assigned *blue-skewed* or *red-skewed* according to the relative peak intensities.

Figure 13 shows some examples of the profiles with classified classes, such as double peak, skew, single, and complex, respectively. As seen in the bottom left panel, *single* may be due to the lack of sensitivity to detect the counterpart. Most *complex* profiles are affected by the multi-velocity components implied by the optically thin tracer, but as shown in the bottom right, there is a core with a single peak in optically thin line but with multiple peaks in optically thick lines.

Figure 14 shows the correlation plot of line classification between HCO^+ and HNC, indicating the good correlation between the two lines, but not always the same. In particular, $\sim 30\%$ of cores showing blue double profile in HNC show red double peak in HCO^+ . This may reflect the contribution from outflow according to the higher chance of spectra with tail/wing structures seen in HCO^+ . Some showing a single peak profile in HNC, which tend to be low-mass or less dense cores, show a skew profile in HCO^+ , implying the initial signature of inward motion is easier to see in HCO^+ than HNC. More detailed discussion of these classifications and cores' physical properties is in Section 4.2.

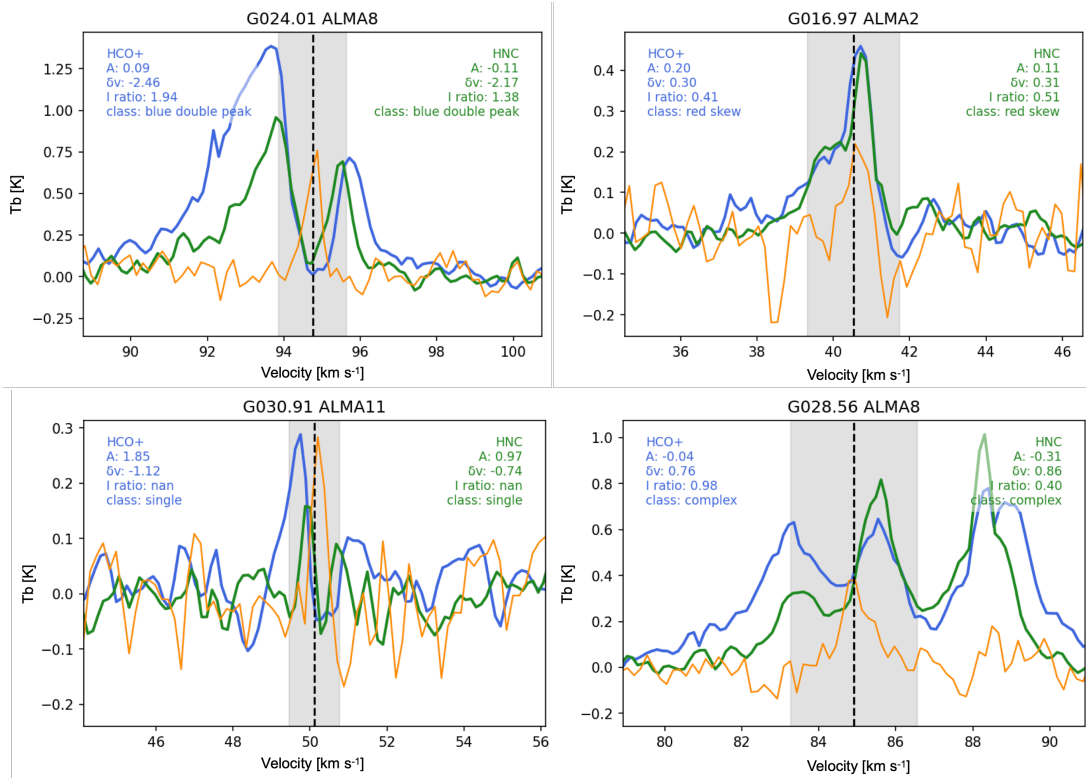


Figure 13. Examples of the profiles for four cores showing various classifications. Blue and green colors represent HCO^+ and HNC , respectively. Orange line represents the optically thin tracer (i.e., DCO^+ or N_2D^+ , which is multiplied by 2 in intensity). V_{thin} is denoted as the black dashed line, and the gray shaded areas show the range where A is calculated ($V_{\text{thin}} - 2\Delta V_{\text{thin}}$).

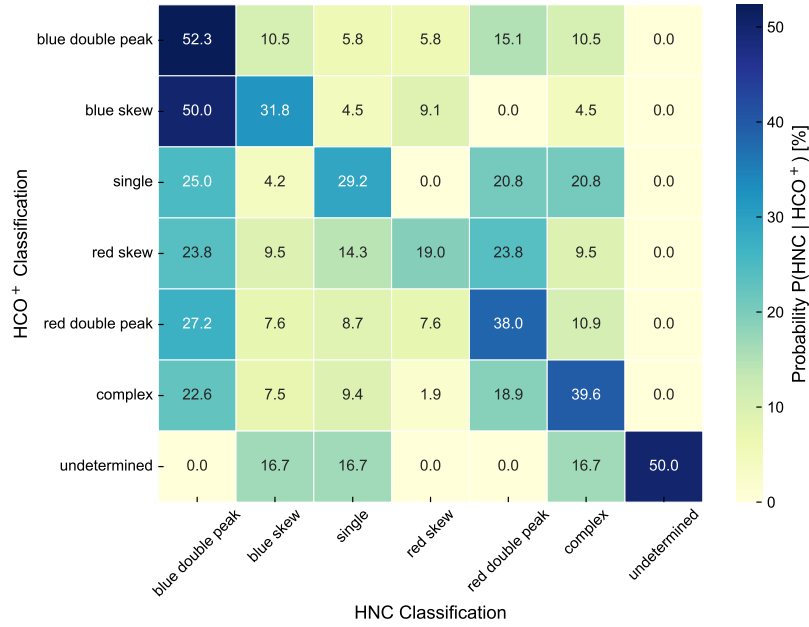


Figure 14. Correlation plot of line classification between HCO^+ and HNC .

D. OPTICAL DEPTH ESTIMATION OF HCO⁺ ($J = 3 - 2$)

To estimate the peak optical depth (τ) of the HCO⁺ ($3-2$) transition, we utilized the rarer isotopologue HC¹⁸O⁺ ($J = 3 - 2$) as an optically thin reference. We analyzed three representative regions (G022.69, G023.47, and G030.91), covering a total of 30 cores that span all line-profile categories discussed in this work (prestellar, protostellar, double-peaked, blue/red-skewed, and single-peaked). Both data sets used the TP+12m+7m combined products. Assuming Local Thermodynamic Equilibrium (LTE), the total column density is given by:

$$N = \frac{8\pi\nu^3}{c^3} \frac{Q(T_{\text{ex}})}{g_u A_{\text{ul}}} \frac{\exp(E_u/T_{\text{ex}})}{[\exp(h\nu/k_B T_{\text{ex}}) - 1]} \int \tau dv \approx \frac{8\pi\nu^3}{c^3} \frac{Q(T_{\text{ex}})}{g_u A_{\text{ul}}} \frac{\exp(E_u/T_{\text{ex}})}{[\exp(h\nu/k_B T_{\text{ex}}) - 1]} \frac{W}{J(T_{\text{ex}}) - J(T_{\text{bg}})} \quad (\text{D1})$$

where the approximation in the second line holds under the optically thin assumption ($\tau \ll 1$) and $J(T) = \frac{h\nu/k_B}{\exp(h\nu/k_B T) - 1}$. Here $W = T_{\text{b,peak}} \Delta v_{\text{FWHM}} \sqrt{\frac{\pi}{4 \ln 2}}$ is the integrated intensity estimated from a Gaussian fit to the HC¹⁸O⁺ line, $T_{\text{b,peak}}$ is the peak brightness temperature, Δv_{FWHM} is the full width at half maximum derived from the Gaussian fit, A_{ul} is the Einstein A coefficient, g_u is the upper-level degeneracy, E_u is the upper-level energy, $Q(T_{\text{ex}})$ is the partition function, and $T_{\text{bg}} = 2.73$ K is the cosmic microwave background temperature. The spectroscopic parameters adopted for HC¹⁸O⁺ ($J = 3 - 2$) are $\nu = 255.488$ GHz, $A_{\text{ul}} = 1.265 \times 10^{-3}$ s⁻¹, $E_u = 24.52$ K, and $g_u = 7$. We adopted the excitation temperature $T_{\text{ex}} = 18.0, 13.9,$ and 12.4 K for G022.69, G023.47, and G030.91, derived from Herschel SED fitting (K. Morii et al. 2023), and assumed that both isotopologues share the same T_{ex} . It should be noted that if the true excitation temperature of HCO⁺ is lower than our assumed T_{ex} , the derived optical depth $\tau(\text{HCO}^+)$ would be underestimated.

The total HCO⁺ column density was obtained by applying the Galactocentric distance-dependent isotopic abundance ratio:

$$\frac{[^{16}\text{O}]}{[^{18}\text{O}]} = 58.8 R_{\text{GC}} (\text{kpc}) + 37.1 \quad (\text{D2})$$

following T. L. Wilson & R. Rood (1994). The adopted Galactocentric distances and resulting abundance ratios are $R_{\text{GC}} = 4.38, 4.19,$ and 5.81 kpc for G022.69, G023.47, and G030.91 (J. S. Whitaker et al. 2017), corresponding to ratios of $\sim 295, \sim 284,$ and ~ 379 , respectively. The peak optical depth was then derived by inverting the standard LTE column density expression:

$$\tau_{\text{HCO}^+} = N_{\text{HCO}^+} / \left[\frac{8\pi\nu^3}{c^3} \cdot \frac{Q(T_{\text{ex}})}{g_u A_{\text{ul}}} \cdot \frac{\exp(E_u/T_{\text{ex}})}{\exp(h\nu/k_B T_{\text{ex}}) - 1} \cdot \Delta v_{\text{FWHM}} \sqrt{\frac{\pi}{4 \ln 2}} \right] \quad (\text{D3})$$

where the spectroscopic parameters for HCO⁺ ($3-2$) are $\nu = 267.566$ GHz, $A_{\text{ul}} = 1.438 \times 10^{-3}$ s⁻¹, $E_u = 25.68$ K, $g_u = 7$, and the partition function is approximated as $Q(T_{\text{ex}}) = 0.4671 T_{\text{ex}} + 0.3445$.

Of the 30 cores analyzed, HC¹⁸O⁺ ($J = 3 - 2$) was detected in 14 cores, yielding optical depths in the range of 1.7–11.4 (mean=6.3), confirming that HCO⁺ ($3-2$) is optically thick across a wide range of core properties. The majority of these detections correspond to cores exhibiting double-peaked HCO⁺ profiles. For the remaining 16 cores where HC¹⁸O⁺ was not detected, we used the 3σ rms noise level of the spectra to derive upper limits, obtaining $\tau_{\text{HCO}^+} < 0.8\text{--}13.7$ (mean upper limit = 6.7). None of the non-detections indicate clearly optically thin conditions, and optical thickness cannot be excluded in any of these cases.

E. INFALL PARAMETERS AND PHYSICAL PARAMETERS

We investigated if there is any correlation between these parameters and cores physical properties. Figure 15 shows the scatter plots of A and δ_v against core mass (left), surface density (middle), and virial parameters (right). Cores with blue asymmetry line profiles (i.e., a blue double peak or blue skew) are shown in color, where color represents the molecule, same as Figure 3. The lines overlaid are regression plots. There is a trend of A -increase as core mass and surface density increase, and a decrease in the virial parameter. The δ_v parameter does not significantly change with core mass, density, and virial parameter. However, there are some trends when all cores are considered (gray triangles for the HNC case). These tendencies imply that more inward motions are seen from more massive, denser, and bound cores, which is consistent with the main conclusion from the main text.

REFERENCES

- Astropy Collaboration, Robitaille, T. P., Tollerud, E. J., et al. 2013, *A&A*, 558, A33, doi: 10.1051/0004-6361/201322068
- Astropy Collaboration, Price-Whelan, A. M., Sipőcz, B. M., et al. 2018, *AJ*, 156, 123, doi: 10.3847/1538-3881/aabc4f

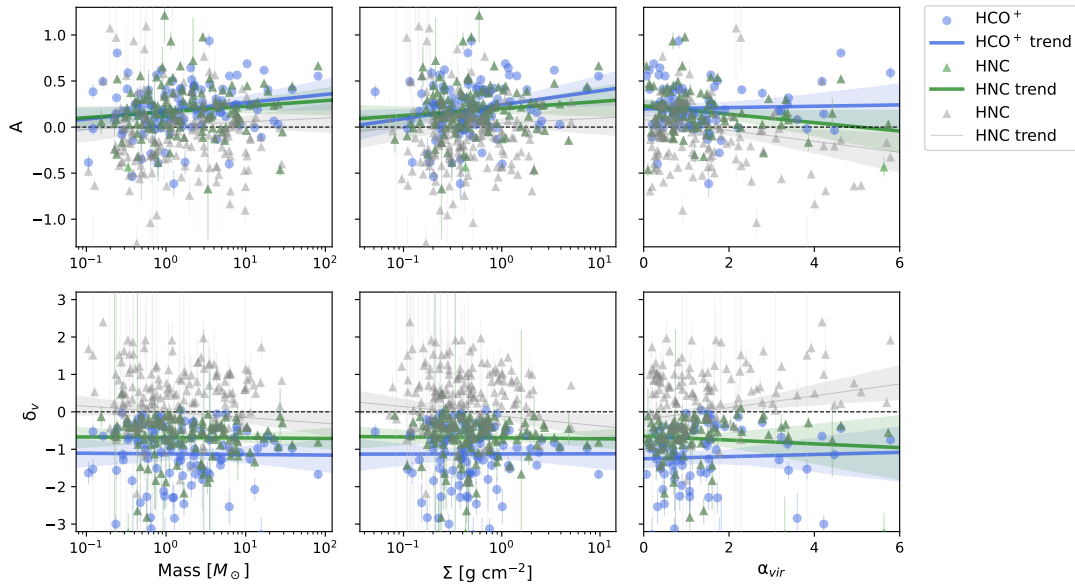


Figure 15. δ_v and A against core mass, surface density, and virial parameter. Colors are the same as Figure 3. Lines are regression plots. Cores with blue asymmetry line profiles (i.e., a blue double peak or blue skew) are shown in color. Gray triangles and regression plots show the parameters of all cores measured by the HNC line.

- Astropy Collaboration, Price-Whelan, A. M., Lim, P. L., et al. 2022, *ApJ*, 935, 167, doi: [10.3847/1538-4357/ac7c74](https://doi.org/10.3847/1538-4357/ac7c74)
- Beuther, H., Linz, H., Tackenberg, J., et al. 2013, *A&A*, 553, A115, doi: [10.1051/0004-6361/201220475](https://doi.org/10.1051/0004-6361/201220475)
- Bonnell, I. A., Vine, S. G., & Bate, M. R. 2004, *MNRAS*, 349, 735, doi: [10.1111/j.1365-2966.2004.07543.x](https://doi.org/10.1111/j.1365-2966.2004.07543.x)
- Campbell, J. L., Friesen, R. K., Martin, P. G., et al. 2016, *ApJ*, 819, 143, doi: [10.3847/0004-637X/819/2/143](https://doi.org/10.3847/0004-637X/819/2/143)
- CASA Team, Bean, B., Bhatnagar, S., et al. 2022, *PASP*, 134, 114501, doi: [10.1088/1538-3873/ac9642](https://doi.org/10.1088/1538-3873/ac9642)
- Chambers, E. T., Jackson, J. M., Rathborne, J. M., & Simon, R. 2009, *ApJS*, 181, 360, doi: [10.1088/0067-0049/181/2/360](https://doi.org/10.1088/0067-0049/181/2/360)
- Chen, H.-R. V., Zhang, Q., Wright, M. C. H., et al. 2019, *ApJ*, 875, 24, doi: [10.3847/1538-4357/ab0f3e](https://doi.org/10.3847/1538-4357/ab0f3e)
- Chira, R.-A., Smith, R. J., Klessen, R. S., Stutz, A. M., & Shetty, R. 2014, *MNRAS*, 444, 874, doi: [10.1093/mnras/stu1497](https://doi.org/10.1093/mnras/stu1497)
- Contreras, Y., Sanhueza, P., Jackson, J. M., et al. 2018, *ApJ*, 861, 14, doi: [10.3847/1538-4357/aac2ec](https://doi.org/10.3847/1538-4357/aac2ec)
- Csengeri, T., Bontemps, S., Schneider, N., Motte, F., & Dib, S. 2011, *A&A*, 527, A135, doi: [10.1051/0004-6361/201014984](https://doi.org/10.1051/0004-6361/201014984)
- De Vries, C. H., & Myers, P. C. 2005, *ApJ*, 620, 800, doi: [10.1086/427141](https://doi.org/10.1086/427141)
- Evans, N. J. 1999, *ARA&A*, 37, 311, doi: [10.1146/annurev.astro.37.1.311](https://doi.org/10.1146/annurev.astro.37.1.311)
- Evans, N. J. 2003, in *SFCHEM 2002: Chemistry as a Diagnostic of Star Formation*, ed. C. L. Curry & M. Fich, 157. <https://arxiv.org/abs/astro-ph/0211526>
- Foster, J. B., Jackson, J. M., Barnes, P. J., et al. 2011, *ApJS*, 197, 25, doi: [10.1088/0067-0049/197/2/25](https://doi.org/10.1088/0067-0049/197/2/25)
- Fuller, G. A., Williams, S. J., & Sridharan, T. K. 2005, *A&A*, 442, 949, doi: [10.1051/0004-6361:20042110](https://doi.org/10.1051/0004-6361:20042110)
- Gómez, G. C., Vázquez-Semadeni, E., & Palau, A. 2021, *MNRAS*, 502, 4963, doi: [10.1093/mnras/stab394](https://doi.org/10.1093/mnras/stab394)
- Gupta, S., Baug, T., Soam, A., et al. 2026, *ApJ*, 999, 180, doi: [10.3847/1538-4357/ae40fd](https://doi.org/10.3847/1538-4357/ae40fd)
- Harris, C. R., Millman, K. J., van der Walt, S. J., et al. 2020, *Nature*, 585, 357, doi: [10.1038/s41586-020-2649-2](https://doi.org/10.1038/s41586-020-2649-2)
- He, Y.-X., Zhou, J.-J., Esimbek, J., et al. 2016, *MNRAS*, 461, 2288, doi: [10.1093/mnras/stw1301](https://doi.org/10.1093/mnras/stw1301)
- Henshaw, J. D., Caselli, P., Fontani, F., Jiménez-Serra, I., & Tan, J. C. 2014, *MNRAS*, 440, 2860, doi: [10.1093/mnras/stu446](https://doi.org/10.1093/mnras/stu446)
- Ho, P. T. P., & Haschick, A. D. 1986, *ApJ*, 304, 501, doi: [10.1086/164184](https://doi.org/10.1086/164184)
- Hunter, J. D. 2007, *Computing in Science and Engineering*, 9, 90, doi: [10.1109/MCSE.2007.55](https://doi.org/10.1109/MCSE.2007.55)
- Ishihara, K., Nakamura, F., Sanhueza, P., & Saito, M. 2025, *A&A*, 695, L25, doi: [10.1051/0004-6361/202452427](https://doi.org/10.1051/0004-6361/202452427)
- Izumi, N., Sanhueza, P., Koch, P. M., et al. 2024, *ApJ*, 963, 163, doi: [10.3847/1538-4357/ad18c6](https://doi.org/10.3847/1538-4357/ad18c6)
- Jackson, J. M., Rathborne, J. M., Foster, J. B., et al. 2013, *PASA*, 30, e057, doi: [10.1017/pasa.2013.37](https://doi.org/10.1017/pasa.2013.37)

- Jackson, J. M., Whitaker, J. S., Rathborne, J. M., et al. 2019, *ApJ*, 870, 5, doi: [10.3847/1538-4357/aaef84](https://doi.org/10.3847/1538-4357/aaef84)
- Jackson, J. M., Whitaker, J. S., Chambers, E., et al. 2026, *ApJ*, 998, 167, doi: [10.3847/1538-4357/ae19eb](https://doi.org/10.3847/1538-4357/ae19eb)
- Kepley, A. A. 2019., Astrophysics Source Code Library, record ascl:1909.001 <http://ascl.net/1909.001>
- Keto, E. R., Ho, P. T. P., & Haschick, A. D. 1988, *ApJ*, 324, 920, doi: [10.1086/165949](https://doi.org/10.1086/165949)
- Lee, C. W., & Myers, P. C. 2011, *ApJ*, 734, 60, doi: [10.1088/0004-637X/734/1/60](https://doi.org/10.1088/0004-637X/734/1/60)
- Leung, C. M., & Brown, R. L. 1977, *ApJL*, 214, L73, doi: [10.1086/182446](https://doi.org/10.1086/182446)
- Li, S., Sanhueza, P., Zhang, Q., et al. 2020, *ApJ*, 903, 119, doi: [10.3847/1538-4357/abb81f](https://doi.org/10.3847/1538-4357/abb81f)
- Li, S., Sanhueza, P., Lu, X., et al. 2022, *ApJ*, 939, 102, doi: [10.3847/1538-4357/ac94d4](https://doi.org/10.3847/1538-4357/ac94d4)
- Li, S., Sanhueza, P., Zhang, Q., et al. 2023, *ApJ*, 949, 109, doi: [10.3847/1538-4357/acc58f](https://doi.org/10.3847/1538-4357/acc58f)
- Lin, S., Feng, S., Sanhueza, P., et al. 2025, *ApJ*, 990, 229, doi: [10.3847/1538-4357/adf208](https://doi.org/10.3847/1538-4357/adf208)
- Lu, X., Zhang, Q., Liu, H. B., et al. 2018, *ApJ*, 855, 9, doi: [10.3847/1538-4357/aaad11](https://doi.org/10.3847/1538-4357/aaad11)
- Mardones, D., Myers, P. C., Tafalla, M., et al. 1997, *ApJ*, 489, 719, doi: [10.1086/304812](https://doi.org/10.1086/304812)
- Menten, K. M., Pillai, T., & Wyrowski, F. 2005, in *Massive Star Birth: A Crossroads of Astrophysics*, ed. R. Cesaroni, M. Felli, E. Churchwell, & M. Walmsley, Vol. 227, 23–34, doi: [10.1017/S1743921305004321](https://doi.org/10.1017/S1743921305004321)
- Morii, K., Sanhueza, P., Csengeri, T., et al. 2025, *ApJ*, 979, 233, doi: [10.3847/1538-4357/ada27f](https://doi.org/10.3847/1538-4357/ada27f)
- Morii, K., Sanhueza, P., Nakamura, F., et al. 2021, *ApJ*, 923, 147, doi: [10.3847/1538-4357/ac2365](https://doi.org/10.3847/1538-4357/ac2365)
- Morii, K., Sanhueza, P., Nakamura, F., et al. 2023, *ApJ*, 950, 148, doi: [10.3847/1538-4357/accea](https://doi.org/10.3847/1538-4357/accea)
- Morii, K., Sanhueza, P., Zhang, Q., et al. 2024, *ApJ*, 966, 171, doi: [10.3847/1538-4357/ad32d0](https://doi.org/10.3847/1538-4357/ad32d0)
- Morii, K., Sanhueza, P., Zhang, Q., et al. 2026, *ApJ*, 997, 155, doi: [10.3847/1538-4357/ae25f6](https://doi.org/10.3847/1538-4357/ae25f6)
- Myers, P. C., Mardones, D., Tafalla, M., Williams, J. P., & Wilner, D. J. 1996, *ApJL*, 465, L133, doi: [10.1086/310146](https://doi.org/10.1086/310146)
- Padoan, P., Pan, L., Juvela, M., Haugbølle, T., & Nordlund, Å. 2020, *ApJ*, 900, 82, doi: [10.3847/1538-4357/abaa47](https://doi.org/10.3847/1538-4357/abaa47)
- Rathborne, J. M., Jackson, J. M., & Simon, R. 2006, *ApJ*, 641, 389, doi: [10.1086/500423](https://doi.org/10.1086/500423)
- Redaelli, E., Bovino, S., Sanhueza, P., et al. 2022, *ApJ*, 936, 169, doi: [10.3847/1538-4357/ac85b4](https://doi.org/10.3847/1538-4357/ac85b4)
- Reiter, M., Shirley, Y. L., Wu, J., et al. 2011, *ApJ*, 740, 40, doi: [10.1088/0004-637X/740/1/40](https://doi.org/10.1088/0004-637X/740/1/40)
- Rygl, K. L. J., Wyrowski, F., Schuller, F., & Menten, K. M. 2013, *A&A*, 549, A5, doi: [10.1051/0004-6361/201219574](https://doi.org/10.1051/0004-6361/201219574)
- Sabatini, G., Bovino, S., Sanhueza, P., et al. 2022, *ApJ*, 936, 80, doi: [10.3847/1538-4357/ac83aa](https://doi.org/10.3847/1538-4357/ac83aa)
- Sakai, T., Sanhueza, P., Furuya, K., et al. 2022, *ApJ*, 925, 144, doi: [10.3847/1538-4357/ac3d2e](https://doi.org/10.3847/1538-4357/ac3d2e)
- Sanhueza, P., Garay, G., Bronfman, L., et al. 2010, *ApJ*, 715, 18, doi: [10.1088/0004-637X/715/1/18](https://doi.org/10.1088/0004-637X/715/1/18)
- Sanhueza, P., Jackson, J. M., Foster, J. B., et al. 2012, *ApJ*, 756, 60, doi: [10.1088/0004-637X/756/1/60](https://doi.org/10.1088/0004-637X/756/1/60)
- Sanhueza, P., Jackson, J. M., Foster, J. B., et al. 2013, *ApJ*, 773, 123, doi: [10.1088/0004-637X/773/2/123](https://doi.org/10.1088/0004-637X/773/2/123)
- Sanhueza, P., Jackson, J. M., Zhang, Q., et al. 2017, *ApJ*, 841, 97, doi: [10.3847/1538-4357/aa6ff8](https://doi.org/10.3847/1538-4357/aa6ff8)
- Sanhueza, P., Contreras, Y., Wu, B., et al. 2019, *ApJ*, 886, 102, doi: [10.3847/1538-4357/ab45e9](https://doi.org/10.3847/1538-4357/ab45e9)
- Sanhueza, P., Girart, J. M., Padovani, M., et al. 2021, *ApJL*, 915, L10, doi: [10.3847/2041-8213/ac081c](https://doi.org/10.3847/2041-8213/ac081c)
- Sanhueza, P., Liu, J., Morii, K., et al. 2025, *ApJ*, 980, 87, doi: [10.3847/1538-4357/ad9d40](https://doi.org/10.3847/1538-4357/ad9d40)
- Schneider, N., Csengeri, T., Bontemps, S., et al. 2010, *A&A*, 520, A49, doi: [10.1051/0004-6361/201014481](https://doi.org/10.1051/0004-6361/201014481)
- Smith, R. J., Longmore, S., & Bonnell, I. 2009, *MNRAS*, 400, 1775, doi: [10.1111/j.1365-2966.2009.15621.x](https://doi.org/10.1111/j.1365-2966.2009.15621.x)
- Smith, R. J., Shetty, R., Beuther, H., Klessen, R. S., & Bonnell, I. A. 2013, *ApJ*, 771, 24, doi: [10.1088/0004-637X/771/1/24](https://doi.org/10.1088/0004-637X/771/1/24)
- Smith, R. J., Shetty, R., Stutz, A. M., & Klessen, R. S. 2012, *ApJ*, 750, 64, doi: [10.1088/0004-637X/750/1/64](https://doi.org/10.1088/0004-637X/750/1/64)
- Sridharan, T. K., Beuther, H., Saito, M., Wyrowski, F., & Schilke, P. 2005, *ApJL*, 634, L57, doi: [10.1086/498644](https://doi.org/10.1086/498644)
- Tafalla, M., Mardones, D., Myers, P. C., et al. 1998, *ApJ*, 504, 900, doi: [10.1086/306115](https://doi.org/10.1086/306115)
- Tafaya, D., Sanhueza, P., Zhang, Q., et al. 2021, *ApJ*, 913, 131, doi: [10.3847/1538-4357/abf5da](https://doi.org/10.3847/1538-4357/abf5da)
- Traficante, A., Fuller, G. A., Billot, N., et al. 2017, *MNRAS*, 470, 3882, doi: [10.1093/mnras/stx1375](https://doi.org/10.1093/mnras/stx1375)
- Vázquez-Semadeni, E., Gómez, G. C., & González-Samaniego, A. 2024, *MNRAS*, 530, 3445, doi: [10.1093/mnras/stae1090](https://doi.org/10.1093/mnras/stae1090)
- Vázquez-Semadeni, E., Palau, A., Ballesteros-Paredes, J., Gómez, G. C., & Zamora-Avilés, M. 2019, *MNRAS*, 490, 3061, doi: [10.1093/mnras/stz2736](https://doi.org/10.1093/mnras/stz2736)
- Wang, P., Li, Z.-Y., Abel, T., & Nakamura, F. 2010, *ApJ*, 709, 27, doi: [10.1088/0004-637X/709/1/27](https://doi.org/10.1088/0004-637X/709/1/27)
- Waskom, M. L. 2021, *Journal of Open Source Software*, 6, 3021, doi: [10.21105/joss.03021](https://doi.org/10.21105/joss.03021)
- Whitaker, J. S., Jackson, J. M., Rathborne, J. M., et al. 2017, *AJ*, 154, 140, doi: [10.3847/1538-3881/aa86ad](https://doi.org/10.3847/1538-3881/aa86ad)
- Wilson, T. L., & Rood, R. 1994, *ARA&A*, 32, 191, doi: [10.1146/annurev.aa.32.090194.001203](https://doi.org/10.1146/annurev.aa.32.090194.001203)

- Wyrowski, F., Güsten, R., Menten, K. M., et al. 2016, *A&A*, 585, A149, doi: [10.1051/0004-6361/201526361](https://doi.org/10.1051/0004-6361/201526361)
- Xie, J.-J., Wu, J.-W., Fuller, G. A., et al. 2021, *Research in Astronomy and Astrophysics*, 21, 208, doi: [10.1088/1674-4527/21/8/208](https://doi.org/10.1088/1674-4527/21/8/208)
- Xu, F., Wang, K., He, Y., et al. 2023, *ApJS*, 269, 38, doi: [10.3847/1538-4365/acfee2](https://doi.org/10.3847/1538-4365/acfee2)
- Yang, Y., Jiang, Z., Chen, Z., Ao, Y., & Yu, S. 2021, *ApJ*, 922, 144, doi: [10.3847/1538-4357/ac22ab](https://doi.org/10.3847/1538-4357/ac22ab)
- Zhang, Q., & Ho, P. T. P. 1997, *ApJ*, 488, 241, doi: [10.1086/304667](https://doi.org/10.1086/304667)
- Zhang, Q., Ho, P. T. P., & Ohashi, N. 1998, *ApJ*, 494, 636, doi: [10.1086/305243](https://doi.org/10.1086/305243)
- Zhou, S., Evans, II, N. J., Koempe, C., & Walmsley, C. M. 1993, *ApJ*, 404, 232, doi: [10.1086/172271](https://doi.org/10.1086/172271)